Hybrid Vine Robot With Internal Steering-Reeling Mechanism Enhances System-Level Capabilities

David A. Haggerty ⓘ, Nicholas D. Naclerio ⓘ, and Elliot W. Hawkes ⓘ

Abstract—Continuum robots have high degrees of freedom and the ability to safely move in constrained environments. One class of soft continuum robot is the "vine" robot. This type of robot extends from its tip by everting or unfurling new material, driven by internal body pressure. Most vine robot examples store new body material in a reel at their base, passing it through the core of the robot to the tip, and like many continuum robots, steer by selectively lengthening or shortening one side of the body. While this approach to steering and material storage lends itself to a fully soft device, it has three key limitations: (i) internal friction of material passing through the core of the robot limits its length in tortuous paths, (ii) body buckling as the robot's body material is re-spooled at the base can prevent retraction, and (iii) constant curvature steering limits the robot's poses and object approach angles in a given workspace. This letter presents a hybrid soft-rigid robotic system comprising a soft vine robot body and a rigid, mobile, internal steering-reeling mechanism (SRM); this SRM is equipped with a reel for material storage, a bending actuator for steering, and is capable of actuating the robot at any point along its length. This hybrid configuration increases reach along tortuous paths, allows retraction, and increases the workspace. We describe the motivation for the device, generate its mathematical models, present its methods of operation, and verify experimentally the models we developed and the performance improvements over previous vine robots.

Index Terms—Modeling, control, and learning for soft robots, mechanism design, soft robot materials and design.

I. INTRODUCTION

THE field of robotics began with rigid robots, whose powerful and precise movements make them invaluable for manufacturing [1], [2]. However, unstructured, sensitive environments such as Fukushima can provide serious challenges [3]. Soft robots' ability to deform and adapt to their environment offer an alternative approach to navigating complex real-world environments.

One such variety, "vine" robots, are of particular interest for negotiating complex environments. First presented in 2003,

skin-eversion robots have taken many forms [4]–[8]. Our work is inspired by a more recent design by [9], capable of navigating cluttered environments autonomously [10], or via teleoperation [11], burrowing through loose media [12], creating deployable structures [13], and achieving complex shapes through intelligent design [14]. Made of a thin-walled membrane inverted inside itself, these robots "grow" when inflated, passing new material through the body to emerge at the tip to achieve extension. Their bodies do not move relative to their surroundings, reducing environmental interaction forces, making them promising candidates for a variety of applications from medical to search and rescue. However, there are three key limitations to many of the current vine robots that we seek to address in this work.

First, internal friction of body material passing through the core of the robot grows exponentially with the total path angle, limiting the robot's length in tortuous paths [15], [16]. Since most vine robots store their body material in a reel at the base [17]–[19], body material has to pass through the entire length of the body from the base to the tip, accumulating friction along the way.

Second, while simply re-spooling material onto the reel at the base can retract the body, the tension in the internal body material causes buckling for long bodies. Ref. [18] identified that this behavior can be prevented by reducing the tension in the internal body material via a tip-based, tethered motor; while retraction is greatly improved, the length restrictions imposed by the internal body material and additional wiring still limit the robot's achievable length.

Finally, constant curvature steering limits the possible poses and tip orientations of the robot, restricting its reachable workspace. Most vine robots have been steered by selectively lengthening or shortening one side of the robot via tendons or artificial muscles [14], [20]–[22]. While this allows entirely soft devices, it restricts turning to approximately constant curvature deformation, reducing its ability to navigate some obstacles. A number of attempts have been made to overcome this limitation, such as tendon actuation coupled with pneumatic shape locking [20]; discrete, reversible body stiffness modulation [19] and mechanical interlocks [9]; and active and programmable heat sealing [23].

What follows is a description of our design concept to address these limitations, a mathematical description of the various behaviors of this device, and the details of our design informed by this modeling. We then verify the models, and present experimental data showing an increase in tortuous path length, an
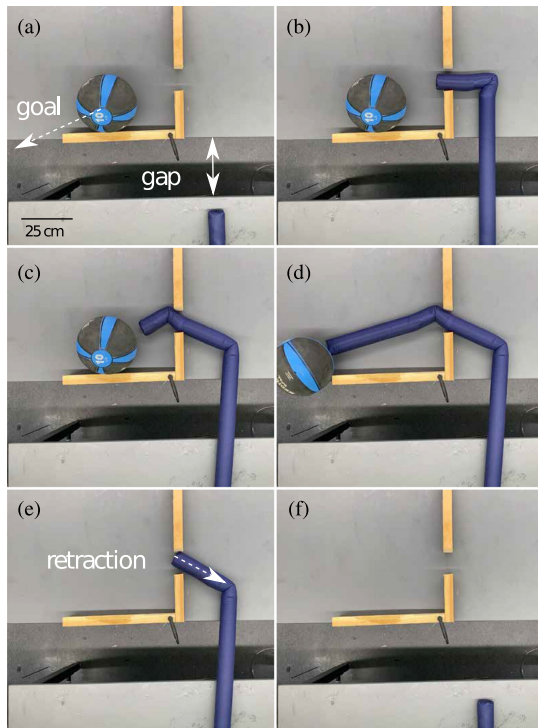
Fig. 1. Overhead view of the presented robot (A) navigating across a gap wider than the internal mechanism (SRM) is long, (B) turning acutely into an opening, (C) turning again to steer at a target object (4.5 kg exercise ball), (D) pushing the ball off of the table, and (E-F) retracting back to its starting location.

integrated retraction ability, and an expanded workspace. We conclude by discussing the potential impacts and future work planned for this new design.

II. CONCEPT

To address length, buckling, and steering limitations, we present a hybrid soft-rigid robotic system (Figs. 1 and 2) comprising a soft vine robot body and a rigid, mobile, internal steering-reeling mechanism (SRM). The SRM is designed to fit inside the vine robot body with sufficient radial clearance to easily allow for sliding and for air to inflate the entire vine robot body, and comprises two segments connected by a revolute joint that can control the vine robot body in two ways. First, it controls robot length by spooling in or out body material that is connected to a reel on the forward or distal segment of the SRM. The proximal tip of the vine robot body is reeled on the SRM spool after passing through the SRM tip as shown in Fig. 2(A). The remainder of the body is everted around the exterior of the SRM as shown in Fig. 2(C). Second, it controls direction by rotating the two sections of the SRM relative to one another to cause a bend in the robot body. The steering motor can bend and hold the robot $120°$ in both directions from the nominal, straight state. This allows point deflections at any point along the robot, creating two arbitrary length segments provided the overall body length constraints are satisfied.

Operation of length and direction control with the SRM is as follows. As shown in Fig. 2(D), when the internal pressure of

the vine robot is low and the spool is fixed, the SRM remains in place due to a small amount of friction between the SRM and the inside of the body. As the spool unreels material (Fig. 2(E)), the robot extends while the SRM remains stationary. When the internal body pressure is increased beyond a threshold pressure, the body everts and pulls the SRM forward (Fig. 2(F)). The SRM then uses the steering motor to create a bend in the body and steer around an obstacle (Fig. 2(G)). Pressure is reduced to keep the SRM in place by friction while the spool is unreeled to lengthen past the obstacle. To advance the SRM again, the reel is locked and pressure is increased to overcome friction, allowing body eversion to pull the SRM toward the tip (Fig. 2(H)). Once the SRM is at a desired location, another turn can be made (Fig. 2(I)). Finally, the robot can retract by reeling in body material while body pressure is low (Fig. 2(J)). Via a series of reeling and unreeling behaviors with high or low pressures, it is possible to achieve any length robot body with the SRM positioned at any location, and from this location it can retract completely to the base by continuously reeling in body material.

The proposed hybrid vine robot concept allows for: i) greater lengths when growing through tortuous paths—total angle of path is no longer bounded due to tail friction, and instead by the length of the robot itself, (ii) retraction regardless of length—the robot can retract at any length when the SRM is moved to the tip, and (iii) a larger workspace—orientation at a given point grows from a single angle for previous designs to a continuous range of up to 115 degrees.

III. MODELING

This section introduces the mathematics that represent the individual elements of the presented concept in comparison to previous vine robots. Our modeling is broken down into three sections: length limitations, retraction, and workspace analysis. This modeling is used to analyze the elements present in Section IV, Design, and verified experimentally in Section V, Results.

A. Length Limitations

The length of a vine robot is limited by the length of the body material on its spool and internal friction. Robots that store body material on a reel at their base pull new material through their body to extend. In straight growth, friction is relatively low, however it increases exponentially with total curvature. This friction, known as capstan friction, is described in [16] as

$$F_{int} = \sum_i C e^{\mu_c \theta_i}, \tag{1}$$

where C is a configuration tension, μ_c is the coefficient of friction in curved growth, and θ_i is the angle of the ith bend. Due to is exponential nature, this friction is very limiting in tortuous paths. The presented concept circumvents this limit by spooling body material at the tip, but is instead bounded by the amount of material that can be fit on the SRM for a given robot diameter.

To understand this volume limitation, we model the spooled tail as a simple Archimedes spiral with a constant rate of radial
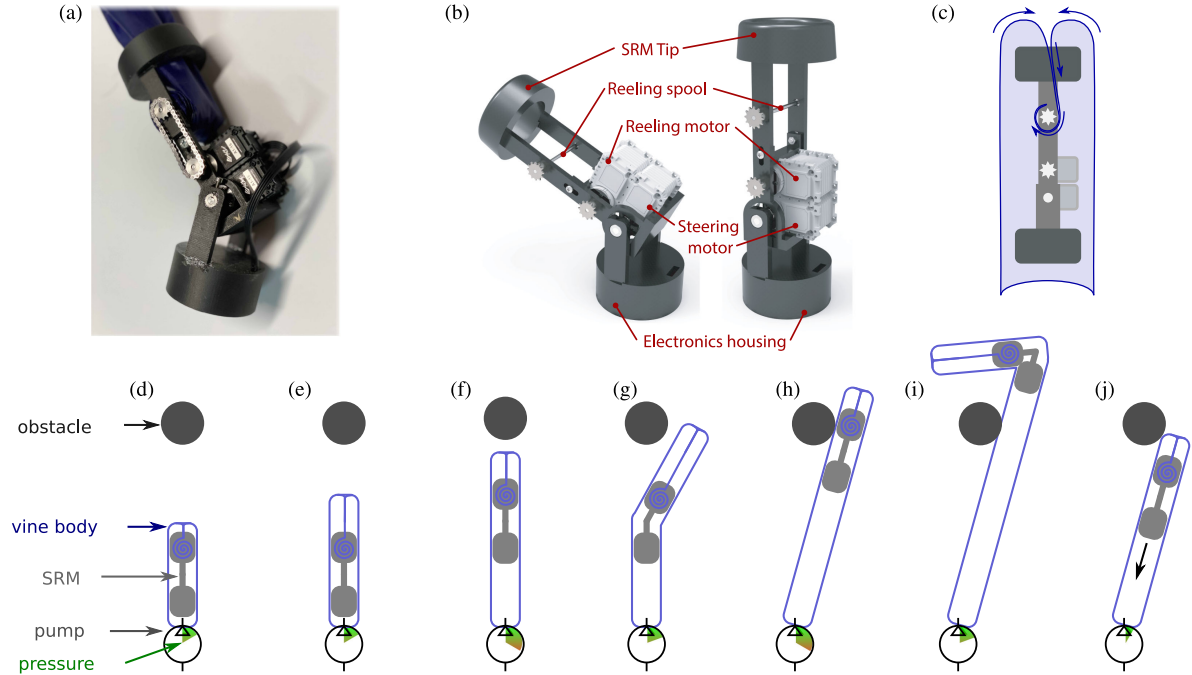
Fig. 2. The SRM (A) controls both the steering and reeling of the external vine robot. Internal actuators enable both steering (B) and length control by reeling (C). The SRM (D) extends the tip of the robot by unreeling new body material (E) while the internal pressure (shown on gauge at bottom) is low. To move the SRM forward to a desired point, the reel is locked and the body pressure is increased so that the friction between the SRM and the robot body is overcome. This allows the everting body to pull the SRM towards the tip of the robot (F). The SRM then bends to steer around an obstacle and unreels more material (G). The reel is again locked and pressure increased to pull the SRM towards the tip of the robot (H), where it makes a new bend (I). It then retracts by reeling in vine body material (J) while it is located at the tip.

expansion, described by

$$r = \alpha a + b, \tag{2}$$

where r is the distance from the center of the spiral to its outermost edge, α is the total swept angle of the spiral, a is a constant such that $2\pi a$ is the separation between two layers of the spiral (i.e. folded tail material thickness), and b is the spiral offset (i.e. the radius of the spooling bar). To understand the limits on robot length, L, we solve for the arc length of the spiral in terms of r and the parameters a and b, denoted $\alpha(r)$, with

$$L = \int_b^{r_{\max}} \sqrt{(\alpha(r))^2 + \left(\frac{d\alpha}{dr}\right)^2} \, dr \tag{3}$$

Using the substitution $u = r - b$, this integral is solved for the maximum length of the robot, $L_{\max}$, as

$$L_{\max} = \frac{1}{a} \left[\frac{(r_{\max} - b)}{2} \sqrt{(r_{\max} - b)^2 + 1} \right.$$

$$\left. + \frac{1}{2} \ln \left(r_{\max} - b + \sqrt{(r_{\max} - b)^2 + 1} \right) \right] \tag{4}$$

where $r_{\max}$ is the radius of the robot body. In our robot, b is much smaller than αa, meaning the second term of (2) will be negligible. We note that (4) shows that L grows with the square of r, yielding nonlinear length increases per unit increase in diameter. As well, the same formulation given in (4) can be

applied in terms of α, such that the length of the robot can be controlled in closed loop with a retraction motor encoder.

B. Retraction, Steering, and SRM Movement

In this section, we first describe the forces required to retract and steer such that we develop the parameters to guide our choice of reeling and steering motors, as described in Section IV. Then, we describe the conditions that determine whether the SRM moves or remains stationary.

1) Force for Retraction: Past retraction work [18] has shown that the force required to invert a vine robot is equal to one half the force produced by pressurization plus a zero pressure offset term (a material-dependent constant that represents the force required to invert or evert material, independent of pressure). Since this new design incorporates an internal component with mass, we modify the formulation given in [18] to incorporate the friction between the robot body and the SRM, becoming

$$F_R \leq \frac{PA}{2} + F_I + F_{fric} \tag{5}$$

where P is the internal pressure, A the cross sectional area, F_I the material dependent constant, and F_{fric} the friction between the SRM and the robot body. Equation (5) is an inequality due to the fact that friction may or may not be present, depending on the retraction condition (the SRM may not be retracting from the tip, and may not be moving relative to the robot body).

Using relationships (2) and (4) to determine the maximum radius of the spool, $r_{\max}$, for a given robot length, we can use

(5) to predict the theoretical maximum torque, τ_R, required to retract the robot, which occurs when the spool is at its largest and the SRM is at the tip. Assuming orthogonality at the point of spooling, we have

$$\tau_R = r_{\max} \times F_R = \left(\frac{1}{2} P_{\max} A + F_I + F_{fric} \right) r_{\max}, \quad (6)$$

where $P_{\max}$ is the maximum pressure commanded to the robot. This model helps in sizing the reeling motor.

2) Limits on Revolute Joint: Similar to Section III-B, we need to understand the forces involved, here for bending of the body, to develop the specifications for the bending motor. Previous work [17], [24] showed that the internal restoring moment, M_{int} produced by an inflatable beam under transverse loading is

$$M_{int} = \pi P r^3, \quad (7)$$

where P is internal pressure and r is the beam radius. The torque requirement for the bending motor is thus

$$\tau_B \geq M_{int,max} = \pi P_{\max} r^3 \quad (8)$$

where τ_B is the minimum bending motor torque for a maximum operational pressure $P_{\max}$. We see in (7) that the internal moment is nominally independent of deflection. This implies that so long as the motor torque exceeds the minimum specification given in (8), the revolute joint can achieve any bending angles the geometry of the SRM allows.

3) SRM Movement: Next, we describe the relationships that govern when the SRM moves versus remains stationary (shown in Fig. 2). It is the balance of three primary forces that determines whether the SRM moves: the tension force on the tail $PA/2$, the inversion/eversion force F_I, and the friction force between the SRM and the inside of the body F_{fric}. The last force can vary depending on the configuration of the SRM, where a straight SRM will have a lower friction force than a bent one. There are two common ways these forces relate, either

$$\frac{PA}{2} > F_{fric} + F_I, \quad \text{or} \quad \frac{PA}{2} < F_{fric} - F_I. \quad (9)$$

In the first case, the pressure is relatively high, and the body will evert, pulling the SRM with it. In the second case, the pressure is relatively low, and the SRM will stay in place and can retract the body if the tail is reeled. There is a third, less common case for moderate pressures, in which $PA/2$ is within $\pm F_I$ of F_{fric}. In this case, retraction of the motor results in motion of the SRM forward, but no retraction of the body.

C. Workspace Analysis

In this section, we explore the two-dimensional space that this robot can achieve when using the proposed actuation modality, and compare and contrast that to the workspace of many previous vine robots that are constrained to a constant curvature of the body.

To date, vine robots have often been actuated by pneumatic artificial muscles (PAMs) or motor-driven tendons, resulting in continuous, distributed deformation along the length of the body. Significant work has been focused on modeling the kinematics
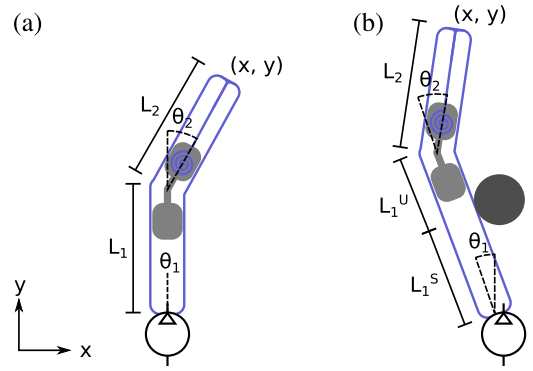

Fig. 3. Geometry of SRM-robot system with (A) and without (B) an obstacle interaction.

of these robots, such as [20]–[22], [25]. Most notably, for a given position in the workspace, these devices are limited to only one approach orientation. This section outlines how the proposed design improves upon this access.

1) Obstacle-Free PRP Kinematics: In this investigation, the kinematics are described by a modified prismatic-revolute-prismatic (PRP) planar rigid robot, as shown in Fig. 3. Essentially, our robot can extend straight from its base, bend at the current location of the SRM, and extend straight from the mechanism to its tip. Williams and Shelley [26] provide the kinematics for this class of planar manipulators, and show the PRP combination to be simply described by

$$E = \begin{bmatrix} x \\ y \end{bmatrix} = A + L_1 e^{j\theta_1} + L_2 e^{j\theta_2}, \quad (10)$$

where (x, y) represents the global frame position, $\phi = \theta_1 + \theta_2$ represents the tip orientation in the base frame, A is a global position offset, L_i is the length of the ith segment, and θ_i its the orientation in the ith frame where $i = 1, 2$.

We note that, for our robot, θ_1 will be zero when there are no obstacles in the workspace (Fig. 3 A). With this θ_1 known, θ_2 is simply the desired tip orientation or approach angle, ϕ.

The lengths L_1 and L_2 are subject to constraints determined by the length of the overall robot, the SRM design, and the robot configuration. Fig. 3 shows the kinematic quantities described in this section, and gives insight into the length constraint. In the zero or one obstacle case, this constraint is described by $L_1 \in [0, L_{\max}]$, and $L_2 \in [0, (L_{\max} - L_1)/2]$ such that $L_1 + L_2 \leq L_{\max} \forall L_1, L_2$. This is due to the fact that at least one half the remaining total body length must be internal to the vine robot to connect to the SRM. That is, for a particular L_1, the remaining body material is $L_{\max} - L_1$, but this material must be split between the everted, external body, and the internal material attached to the SRM, yielding the constraint $L_2 \leq (L_{\max} - L_1)/2$.

2) N Obstacle PRP Kinematics: If the robot instead grows around multiple obstacles successively, the analysis can be extended to a multi-link robot. Generally, the robot can be described as functionally having $n + 1$ prismatic links, where n is the number of obstacles with which it interacts. In these cases, the kinematics given in (10) can be extended with n links of

known lengths and angles, and the length constraint given above can also be generalized by cascading the above relationship into $n + 1$ segments.

When a single obstacle support occurs, θ_1 is known and constant. We then cut L_1 into the supported length and the unsupported length, denoted L_1^s and L_1^u, respectively, with $L_1 = L_1^s + L_1^u$. The length constraint then becomes $L_1 \in [L_1^s, L_{\max}]$ and $L_2 \in [0, (L_{\max} - L_1)/2]$ (Fig 3 B). For n obstacles, we recognize θ_i, $i \in [1, n]$, is known and constant, and that each obstacle interaction defines the length of that link to be L_i^s, $i \in [1, n-1]$ (because the uncontrolled links between obstacles will take the shortest possible path). Thus, we can extend the length constraint to become $L_n \in [L_n^s + \sum_{i=1}^{n-1} L_i, L_{\max}]$, $L_{n+1} \in [0, (L_{\max} - L_n)/2]$. Once each prismatic joint length and its associated angle is defined, the generalized kinematics become

$$E = \begin{bmatrix} x \\ y \end{bmatrix} = A + \sum_{i=1}^{n} L_i^s e^{j\theta_i} + L_{n+1} e^{j\theta_{n+1}}. \qquad (11)$$

It is important to note here that the robot remains fully defined, as each object interaction in a given series can occur at only one angle in the global frame, with the lengths of each supported link known.

3) Reachable Workspace: Finally, (11) allows us to determine the reachable workspace. The nominal workspace (i.e. with no obstacles) can be described by $\mathcal{W}_\circ = \{(x, y) | \theta_1 = 0, \theta_2 \in \Theta_2, L_1 + L_2 \leq L_{\max}\}$, where Θ_2 is set by the robot joint limits. When obstacle support occurs, we utilize the length and angle constraints given in the previous section. From this formulation we can generalize the obstacle interaction subspaces as $\mathcal{W}_i = \{(x, y) | \theta_i \in \Theta_i, \theta_{i+1} \in \Theta_{i+1}, \sum_i^{i+1} L_i \leq L_{\max}\}$, where Θ_i is the obstacle support angle in the local frame and Θ_{i+1} defines the range of joint angles. Finally, we can describe the total workspace, $\mathcal{W}_t$, as $\mathcal{W}_t = \mathcal{W}_\circ \bigcup_{i=1}^{n} \mathcal{W}_i$.

Fig. 4 A shows a representative workspace with no obstacles present. The limits of the motion of the SRM's bending actuator are set to $\pm 105^o$, according to the design of the device, and the total length of the robot material is set to unity with L_i described as a percentage of total length. Interestingly, the further distal the SRM and thus the reel of material, the further the reach of the robot, as described by the length relationships above. That is, in the case where $L_1 = 0$ (green), the robot body material must extend from the reel internally to the tip and back to the base externally. However, for the case where $L_1 = 66$, the internal material only needs to reach from the SRM to the tip, as depicted in Fig. 3. Fig. 4 B shows how the workspace changes when the robot interacts with an obstacle. Since the robot body is able to anchor on an obstacle, the SRM is able to travel forward while the base angle, θ_1, remains locked. This means the robot can reach further in the direction beyond the obstacle than when the obstacle was not present.

The robot can also achieve new approach angles when anchored to the obstacle. Fig. 5 presents the range of tip orientations at each point within the workspace for the case of one obstacle. While many areas of the workspace can be reached with over ninety degrees of tip orientations for our robot, we
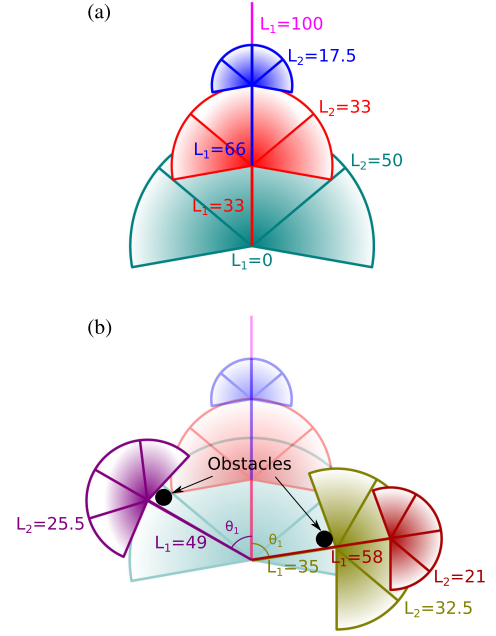

Fig. 4. Theoretical workspace for the robot. While the robot's actual length is 2.4 m, lengths here are represented as relative percentages. (A) With no obstacles present, the robot is able to grow forward and make a single turn at various lengths, L_1. The behavior is similar to a PRP planar manipulator. (B) With the addition of obstacles, the robot can hold a new base angle, θ_1, to open up new tip orientations in the workspace.
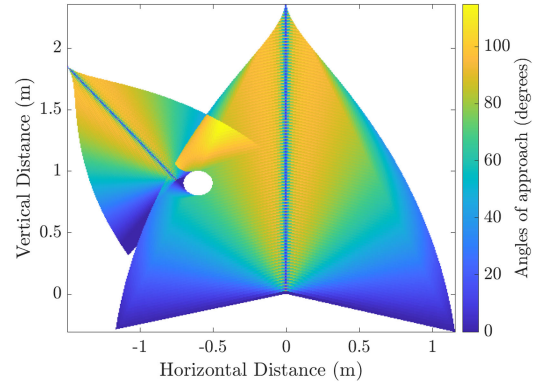

Fig. 5. Theoretical heatmap of tip orientations for a workspace that includes a single obstacle.

note that a constant curvature robot can only reach most areas with a single approach angle, besides near the obstacle, where two discrete angles are possible [21].

IV. ROBOT DESIGN

A. Parameter Selection and Scaling

To chose the parameters for our robot, we begin by choosing an arbitrary desired length, which we set to 2.4 m. From this, we used (4) to determine that the maximum spool diameter is required to be 42 mm to hold this amount of material. This recognizes that the tail material must fold at least once to fit inside the robot because the half circumference width of a "lay flat" state is wider than the diameter. After including the dimensions of the drivetrain and SRM frame, we found that the

minimum robot diameter is 68 mm. This in turn allowed us to use (6) to calculate the required reeling motor torque to be 0.30 Nm using the value of F_{fric} reported in Section V-C. We then used (8) to calculate the required steering motor torque to be 0.84 Nm.

More generally, we describe how these parameters scale. First, we note that from (4) we know that the maximum length the robot can achieve grows as the square of the spool radius. Since the spool must fit inside the robot, this also means length grows as the square of robot radius. Next, we note that the required motor torque to retract the robot body grows as the cube of the radius (6), and the motor torque required to steer the body also scales as the cube of radius (8). Since motor torque scales with volume ($\sim r^3$), these three scaling laws suggest that a larger robot will be able to grow proportionally longer, and that the required relative size of the internal motors will remain the same regardless of scale.

B. Fabrication

With these specifications, we built a hybrid robot, composed of two parts, the soft robot skin and the rigid SRM that rides inside the robot skin as shown in Fig. 2.

The skin is made of a 71 μm thick silicone-urethane impregnated ripstop nylon fabric (Rockywoods Fabric) tube with an 75 mm diameter, and 2.5 m length. The tube is made by from a strip of fabric using a lap joint, bonded with room temperature vulcanizing silicone adhesive (Smooth-on Silpoxy) as in [27]. The 70 mm diameter SRM is made of two 3D printed Markforged Oynx (chopped carbon fiber-impregnated nylon filament) frames connected by an actuated hinge joint. The 150 mm long distal segment contains a reel of up to 3 m of vine robot skin and the bending mechanism, while the 80 mm long proximal segment houses the batteries and wireless transmitter; when assembled, the entire SRM is 215 mm long. The vine body material reel is a 3 mm diameter steel rod mounted to the frame perpendicular to the length of the robot body. Given the required torque, we chose an XYZrobot Smart Servo a1-16 motor with a rated torque of 2.5 Nm; its output drives the reel via a small steel chain. The joint of the robot is rotated by a second, inline XYZrobot Smart Servo a1-16 motor, also rated to 2.5 Nm, and the joint can achieve rotations up to $120°$ in the positive right-hand direction, and $105°$ in the negative right-hand direction (with the difference due to geometrical constraints imposed by the actuator's construction). The motors are powered by three 500mAh, 3.7 V lithium-polymer batteries, controlled by an Adafruit Feather M0 interfaced with 915 MHz radio. When fully assembled SRM has a mass of 337.5 g.

V. RESULTS

Here we discuss testing of length limitations and the reachable workspace of our robot.

A. Length Limitations

We first present test results comparing the performance of our robot to a vine robot with the reel at the base on a tortuous
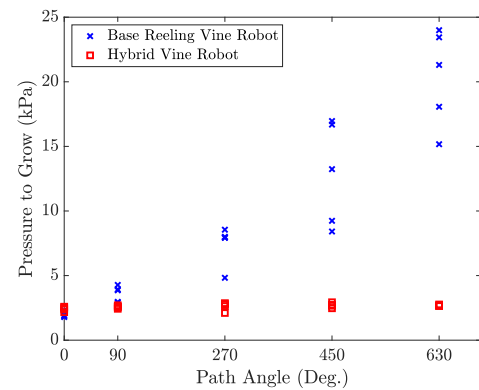

Fig. 6. Pressure required to grow through tortuous paths. With the body material reeled at the base, as is common in previous vine robots, the pressure to grow increases with path angle. In contrast, for the presented robot with the body material reeled in the SRM, the pressure to grow remains roughly constant when the SRM is near the tip.

path. Second, we test our model of the relationship among spool angle, spooled material radius, and robot length.

1) Increased Length Along Tortuous Paths: From (1), for previous vine robot designs with the reel in the base, we expect the internal pressure to increase exponentially with the total angle of a tortuous path, as the tail pulls through the inside the curved body. In contrast, for the presented robot, we predict a near constant pressure across length. To test this, we measured the pressure to grow for a robot in a serpentine path, constrained by a series of pegs in two rows, 30 cm apart with a peg spacing of 28 cm. Two robots of roughly equal diameter—one with base spooling, one with an SRM—were tested. Each robot was placed in the test set up around a given number of pegs, then the pressure was increased until growth occurred. To bend around the first peg required a turn of $90°$, and an additional $180°$ for every subsequent peg, up to a total path angle of $630°$. The test was repeated five times with each robot design. The results presented in Fig. 6 show that at a $0°$ path angle, the pressure required to grow the vine robot with the reel at its base is similar, or slightly lower, than required for the SRM. As path angle increases, the pressure to grow with the SRM remains constant, but increases exponentially for the robot with the reel at its base, as expected by (1). Thus, the presented design is only length-limited by the constraints imposed in Section III-A.

B. Spool Geometry

First, we sought to determine the value of a in (2), which is nominally the thickness of material in each wrap of the tail divided by 2π. Since the flat tail material is wider than the diameter of the robot (equal to half the robot circumference), it must fold at least once to fit on the reel, meaning a must be at least $4t/2\pi$, with t being the thickness of one layer of material. In reality, a will be larger than this, due to wrinkling and air gaps. To determine a experimentally, we reeled the tail while measuring the angle of the reel and its radius (Fig. 7). The actual packing density was 57.2% of the theoretical limit.

Second, using the measured a, we compared the predicted length versus spool radius from (4) to experimental data (Fig. 8). While trends match, the model slightly underestimates the actual
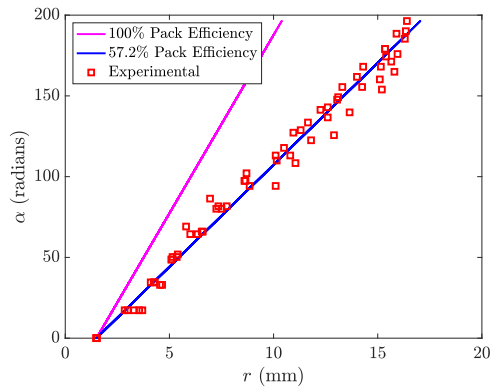
Fig. 7. Experimental results used to determine the actual value of a for (2). A best fit line (blue) suggests that the value of a is approximately 57.2% of the theoretical packing density limit (magenta).
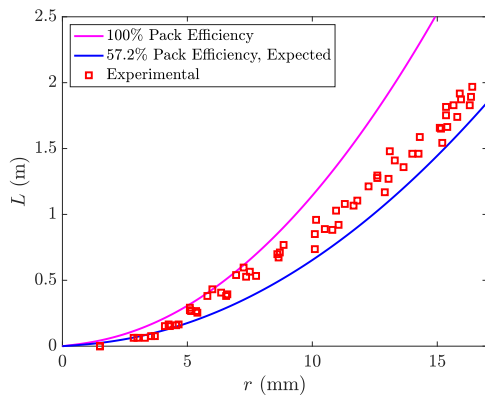

Fig. 8. Experimental testing of the spiral model (4) shown with the expected curve (blue) using the value of a from Fig. 7, as well as the theoretical limit with perfect packing.

length of material on the reel, possibly because the material is not perfectly straight on the reel.

C. SRM Movement

In this section, we determine the bounds on (9) in Section III-B3 to understand the expected behavior of the SRM at various pressures. We ran five trials each to determine F_{fric} and F_I, using a Mark-10 $100\,N$ push/pull force gauge. To determine F_{fric}, the SRM was detached from the vine robot body and pulled along a strip of body material with the force gauge just until sliding occurred, with the peak force recorded. The average value was found to be $0.65\,N$, with a standard deviation of $\pm 0.05\,N$. A similar test was conducted to determine F_I; with the tail of the material attached to the force gauge, it was pulled until inversion just began, recording the peak force. The average value was found to be $0.30 \pm 0.05\,N$.

Applying (9), we predicted that the SRM would be pulled to the tip at pressures exceeding $0.41\,kPa$. To verify this expectation, tail material was spooled off of the SRM at zero pressure and it was positioned in the center of the robot body. Pressure was slowly increased, and the measurement was recorded when sustained movement was observed. The average pressure across five tests was found to be $0.39 \pm 0.04\,kPa$.
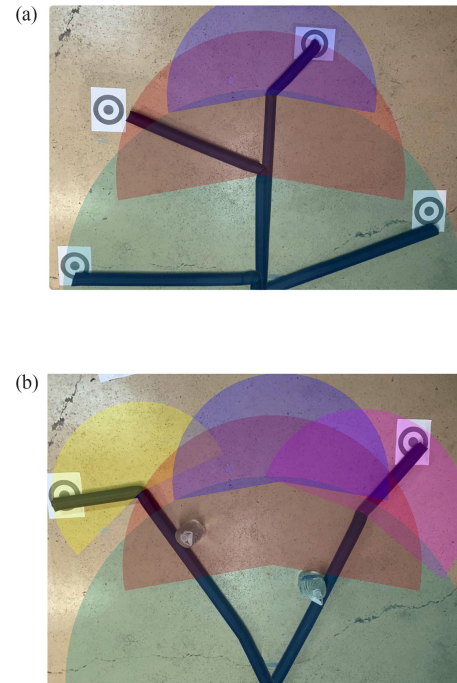

Fig. 9. Experimental validation of theoretical workspace. (A) No obstacles. (B) With two obstacles. Reachable workspace arcs at each bending position, from (11) are overlaid.

We note that this pressure limitation greatly slows the operation of the device, and future work is planned to incorporate a braking device into the design such that this feature of controllable SRM position and relative motion may be better utilized in the robot's operation.

D. Workspace

To help verify our model of the robot workspace, we grew the robot in a series of tests while recording position in the plane via an overhead video camera. We first tested reachable workspace with and without obstacles. The results of these experiments are shown in Fig. 9. While small discrepancies exist, the expected trends are observed: in the no-obstacle case, lateral reach is reduced as the SRM moves more distally (Fig. 9(A)), and the addition of obstacles extends the workspace in the region beyond the obstacle (Fig. 9(B)). We then tested the range of tip orientations at three target points in the workspace for a single obstacle case, with results shown in Fig. 10. Again, the expected trends are observed. Limited tip orientations are found at the extent of the workspace (bottom right target), close to 80 degrees of tip orientations are available away from the obstacle (leftmost target), and almost 130 degrees are achievable near the obstacle (middle target). While the model presented in Fig. 5 predicts approximately $110°$, accounting for the asymmetry in the actual device in the model yields exactly the results observed.

VI. DISCUSSION AND CONCLUSION

We have presented a hybrid soft-rigid robot, comprising a compliant vine robot and a rigid internal steering and reeling mechanism (SRM). This new design overcomes three key
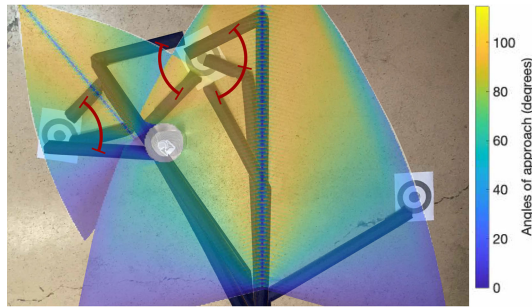
Fig. 10. Experimental validation of theoretically achievable tip orientations when there is a single obstacle in the workspace. A heat map of achievable tip orientations as modeled in Fig. 5 is overlaid.

limitations of past constant curvature vine robots with base-mounted reels: length restrictions due to internal friction, retraction bounds on free robot lengths and poses, and workspace limitations due to constant curvature kinematics. We have shown that incorporating an SRM in a vine robot eliminates length restrictions caused by friction, enables retraction in any pose, and increases the achievable angles of approach by orders of magnitude.

These improvements may advance the performance of vine robots in real-world applications. For example, the improved workspace could enable robots to better navigate difficult archaeology sites [11], aircraft interiors, or nuclear facilities. Reduced internal friction by tip spooling could also enable vine robots to access more tortuous paths, such as the small intestine, machinery, or animal burrows. The SRM however, reduces growth speed and limits the vine robot's ability to squeeze through gaps smaller than the diameter of the SRM. The additional weight also makes it more difficult to span gaps.

The development of the SRM offers many opportunities for future work. Adding an additional bending actuator in the same SRM would enable three dimensional steering. Further, with some modification, additional SRMs could be incorporated to create multiple bends in multiple planes at multiple locations along the body. The thoughtful introduction of an end effector such as [9], [11], [28] would also expand the robot's usefulness. In addition, exploring the limits of down scaling the tip spool design would be useful for small-scale applications.

REFERENCES

[1] D. Trivedi, C. D. Rahn, W. M. Kier, and I. D. Walker, "Soft robotics: Biological inspiration, state of the art, and future research," *Appl. Bionics Biomech.*, vol. 5, no. 3, pp. 99–117, 2008.

[2] C. Laschi, B. Mazzolai, and M. Cianchetti, "Soft robotics: Technologies and systems pushing the boundaries of robot abilities," *Sci. Robot.*, vol. 1, no. 1, 2016, Art. no. eaah3690.

[3] T. Yoshida, K. Nagatani, S. Tadokoro, T. Nishimura, and E. Koyanagi, "Improvements to the rescue robot quince toward future indoor surveillance missions in the fukushima daiichi nuclear power plant," in *Field and Service Robotics*, Springer, 2014, pp. 19–32.

[4] D. Mishima, T. Aoki, and S. Hirose, "Development of pneumatically controlled expandable arm for search in the environment with tight access," in *Field Service Robot.*, Springer, 2003, pp. 509–518.

[5] T. Viebach, F. Pauker, G. Buchmann, G. Weiglhofer, and R. Pauker, "Everting Sleeve System," Patent, Jul. 5, 2006, European Patent 1676598A2. [Online]. Available: https://patents.google.com/patent/EP1676598A2/en?assignee=invendo&oq=invendo&sort=old

[6] H. Tsukagoshi, N. Arai, I. Kiryu, and A. Kitagawa, "Smooth creeping actuator by tip growth movement aiming for search and rescue operation," in *Proc. IEEE Int. Conf. Robot. Automat.*, 2011, pp. 1720–1725.

[7] H. Tsukagoshi, N. Arai, I. Kiryu, and A. Kitagawa, "Tip growing actuator with the hose-like structure aiming for inspection on narrow terrain," *IJAT*, vol. 5, no. 4, pp. 516–522, 2011.

[8] A. Sadeghi, A. Tonazzini, L. Popova, and B. Mazzolai, "Robotic mechanism for soil penetration inspired by plant root," in *Proc. IEEE Int. Conf. Robot. Automat.*, 2013, pp. 3457–3462.

[9] E. W. Hawkes, L. H. Blumenschein, J. D. Greer, and A. M. Okamura, "A soft robot that navigates its environment through growth," *Sci. Robot.*, vol. 2, no. 8, 2017, Art. no. eaan3028.

[10] J. D. Greer, L. H. Blumenschein, A. M. Okamura, and E. W. Hawkes, "Obstacle-aided navigation of a soft growing robot," in *Proc. IEEE Int. Conf. Robot. Automat.*, 2018, pp. 1–8.

[11] M. M. Coad *et al.*, "Vine robots: Design, teleoperation, and deployment for navigation and exploration," *IEEE Robot. Automat. Maga.*, vol. 27, no. 3, pp. 120–132, Sep. 2020.

[12] N. D. Naclerio, C. Hubicki, Y. Aydin, D. Goldman, and E. Hawkes, "Soft robotic burrowing device with tip-extension and granular fluidization," in *Proc. IEEE Int. Conf. Intell. Robots Syst.*, 2018, pp. 5918–5923.

[13] H. Godaba, F. Putzu, T. Abrar, J. Konstantinova, and K. Althoefer, "Payload capabilities and operational limits of eversion robots," in *Proc. Annu. Conf. Towards Auton. Robotic Syst.*, 2019, pp. 383–394.

[14] L. H. Blumenschein, L. T. Gan, J. A. Fan, A. M. Okamura, and E. W. Hawkes, "A tip-extending soft robot enables reconfigurable and deployable antennas," *IEEE Robot. Automat. Lett.*, vol. 3, no. 2, pp. 949–956, Apr. 2018.

[15] D. A. Haggerty, N. D. Naclerio, and E. W. Hawkes, "Characterizing environmental interactions for soft growing robots," in *Proc. IEEE/RSJ Int. Conf. Intell. Robots Syst.*, 2019, pp. 3335–3342.

[16] L. H. Blumenschein, A. M. Okamura, and E. W. Hawkes, "Modeling of bioinspired apical extension in a soft robot," in *Proc. Conf. Biomimetic Biohybrid Syst.*, 2017, pp. 522–531.

[17] Z. M. Hammond, N. S. Usevitch, E. W. Hawkes, and S. Follmer, "Pneumatic reel actuator: Design, modeling, and implementation," in *Proc. IEEE Int. Conf. Robot. Automat*, 2017, pp. 626–633.

[18] M. M. Coad, R. P. Thomasson, L. H. Blumenschein, N. S. Usevitch, E. W. Hawkes, and A. M. Okamura, "Retraction of soft growing robots without buckling," *IEEE Robot. Automat. Lett.*, vol. 5, no. 2, pp. 2115–2122, Apr. 2020.

[19] B. H. Do, V. Banashek, and A. M. Okamura, "Dynamically reconfigurable discrete distributed stiffness for inflated beam robots," 2020 IEEE International Conference on Robotics and Automation (ICRA), pp. 9050–9056,, 2020.

[20] S. Wang, R. Zhang, D. A. Haggerty, N. D. Naclerio, and E. W. Hawkes, "A dexterous tip-extending robot with variable-length shape-locking," 2020 IEEE International Conference on Robotics and Automation (ICRA), pp. 9035–9041,, 2020.

[21] M. Selvaggio, L. Ramirez, N. Naclerio, B. Siciliano, and E. Hawkes, "An obstacle-interaction planning method for navigation of actuated vine robots," in *Proc. IEEE Int. Conf. Robot. Automat.*, 2020, pp. 3227–3233.

[22] J. D. Greer, T. K. Morimoto, A. M. Okamura, and E. W. Hawkes, "A soft, steerable continuum robot that grows via tip extension," *Soft Robot.*, vol. 6, no. 1, pp. 95–108, 2018.

[23] Y. Satake, A. Takanishi, and H. Ishii, "Novel growing robot with inflatable structure and heat-welding rotation mechanism," *IEEE/ASME Trans. Mechatronics*, vol. 25, no. 4, pp. 1869–1877, Aug. 2020.

[24] R. Comer and S. Levy, "Deflections of an inflated circular-cylindrical cantilever beam," *AIAA J.*, vol. 1, no. 7, pp. 1652–1655, 1963.

[25] A. Ataka, T. Abrar, F. Putzu, H. Godaba, and K. Althoefer, "Model-based pose control of inflatable eversion robot with variable stiffness," *IEEE Robot. Automat. Lett.*, vol. 5, no. 2, pp. 3398–3405, Apr. 2020.

[26] R. Williams and B. H. Shelley, "Inverse kinematics for planar parallel manipulators," in *Proc. ASME Des. Tech. Conf.*, 1997, pp. 14–17.

[27] N. D. Naclerio and E. W. Hawkes, "Simple, low-hysteresis, foldable, fabric pneumatic artificial muscle," *IEEE Robot. Automat. Lett.*, vol. 5, no. 2, pp. 3406–3413, Apr. 2020.

[28] S.-G. Jeong *et al.*, "A tip mount for transporting sensors and tools using soft growing robots," 2020 IEEE/RSJ International Conference on Intelligent Robots and Systems (IROS), pp. 8781–8788,, 2020, doi: 10.1109/IROS45743.2020.9340950